

# A MULTISPECTRAL QUANTUM DOT INFRARED PHOTODETECTOR

BY

JARROD N. VAILLANCOURT

B.S. UNIVERSITY OF MASSACHUSETTES LOWELL (2006)

SUBMITTED IN PARTIAL FULFILLMENT OF THE REQUIREMENTS

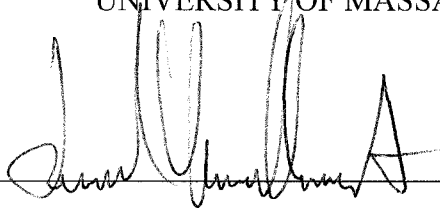
FOR THE DEGREE OF MASTER OF SCIENCE

DEPARTMENT OF ELECTRICAL AND COMPUTER ENGINEERING

UNIVERSITY OF MASSACHUSETTES LOWELL

Signature of

Author:

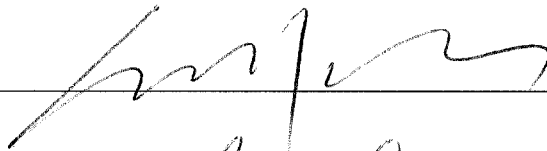


Date:

11/20/07

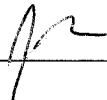
Signature of Thesis

Supervisor:



Signatures of Other Thesis

Committee Members:



UMI Number: 1452638

## INFORMATION TO USERS

The quality of this reproduction is dependent upon the quality of the copy submitted. Broken or indistinct print, colored or poor quality illustrations and photographs, print bleed-through, substandard margins, and improper alignment can adversely affect reproduction.

In the unlikely event that the author did not send a complete manuscript and there are missing pages, these will be noted. Also, if unauthorized copyright material had to be removed, a note will indicate the deletion.



---

UMI Microform 1452638

Copyright 2008 by ProQuest LLC.

All rights reserved. This microform edition is protected against unauthorized copying under Title 17, United States Code.

ProQuest LLC  
789 E. Eisenhower Parkway  
PO Box 1346  
Ann Arbor, MI 48106-1346

# A MULTISPECTRAL QUANTUM DOT INFRARED PHOTODETECTOR

BY

JARROD N. VAILLANCOURT

ABSTRACT OF A THESIS SUBMITTED TO THE FACULTY OF THE  
DEPARTMENT OF ELECTRICAL AND COMPUTER ENGINEERING  
IN PARTIAL FULFILLMENT OF THE REQUIREMENTS  
FOR THE DEGREE OF  
MASTER OF SCIENCE  
UNIVERSITY OF MASSACHUSETTES LOWELL  
(2007)

Thesis Supervisor: Xuejun Lu, Ph.D.

Assistant Professor, Department of Electrical and Computer Engineering

## **ABSTRACT**

Multispectral infrared photodetectors have many applications in both civilian and defense related application. A quantum dot infrared photodetector that consists of vertically-stacked InAs quantum dots layers has been developed. The detection bands have were designed with capping layers of GaAs and  $\text{In}_{0.15}\text{Ga}_{0.85}\text{As}$  for near longwave infrared (NLWIR, 6-8  $\mu\text{m}$ ) and longwave infrared (LWIR, 8-12  $\mu\text{m}$ ) bands, respectively. Voltage-tunable single or dual band operations were demonstrated with over ten times photoresponsivity and photodetectivity  $D^*$  differentiation. Since each of the detection bands can be designed individually and then stacked. Vertically-stacked QDIP structures offer flexibility in detection band engineering and allows easy control of detection bands. The vertically stacked structure can be readily scaled up for multi-band detection.

## **ACKNOWLEDGEMENTS**

I would like to first thank Professor Lu for the knowledge and guidance he has shared over the past two years. The research opportunities that he has provided have continually challenged my abilities, making me into a better engineer, for that I am sincerely grateful.

Next, I would like to also thank the committee members, Professor Armiento and Professor Therrien for their time and effort in reviewing my thesis and providing valuable suggestions.

Finally, I would like to thank my parents who have given me their love and infinite support, along with my fiancée Kate who has stood beside me through all the challenges in my life and provided constant encouragement.

## **TABLE OF CONTENTS**

List of Tables.....	vi
List of Figures.....	vii
I. INTRODUCTION.....	1
1.1 What is Infrared Light.....	1
1.2 Applications of Infrared Detectors.....	3
1.3 Current Detector Technologies.....	5
1.3.1 Thermal Detectors.....	6
1.3.2 Photon Detectors.....	8
II. PHYSICS OF OPERATION.....	15
2.1 Interband vs Intersubband Transitions.....	15
2.2 Multispectral Operation.....	17
III. GROWTH AND FABRICATION.....	19
3.1 Molecular Beam Epitaxy Growth.....	19
3.2 Growth Conditions.....	21
3.3 Photoluminescence .....	23
3.4 Fabrication Procedure.....	25
IV. EXPERIMENTAL SETUP AND RESULTS .....	28
4.1 Photocurrent Spectrum.....	28
4.2 Dark Current.....	30
4.3 Noise Current.....	31
4.4 Photoconductive Gain.....	33
4.5 Responsivity.....	34
4.6 Detectivity.....	38

VI. SUMMARY OF RESULTS.....	40
VII. LITERATURE CITED.....	40

## **LIST OF TABLES**

Table 1.1: Energy gap of common semiconductors.....	10
---	----



## **LIST Of FIGURES**

Figure 1.1: Spectral radiance of a blackbody source at $T=1000\text{K}$ .....	1
Figure 1.2: Atmospheric transmission of IR light.....	2
Figure 1.3: Comparison of a constellation using (a) visible and (b) infrared light.....	3
Figure 1.4: Comparison of (a) visible and (b) infrared images.....	3
Figure 1.5: Diagram of a simple thermal detector.....	6
Figure 1.6: Diagram of photon absorption in a semiconductor .....	8
Figure 1.7: Graph of photon energy versus wavelength .....	9
Figure 1.8: Graph of energy gap of $\text{HgCdTe}$ as a function of cadmium content.....	11
Figure 1.9: Diagram of Auger recombination mechanism.....	11
Figure 1.10: Simplified diagram of intersubband transition .....	12
Figure 1.11: Diagram of a quantum well infrared photodetector .....	13
Figure 2.1: (a) Bulk GaAs and (b) energy band diagram for bulk GaAs showing the closely spaced energy levels in conduction band.....	15
Figure 2.2: (a) Quantum well structure and (b) energy levels.....	16
Figure 2.3: (a) Structure of quantum dot and (b) energy levels.....	16
Figure 2.4: Conduction band energies under (a) small and (b) large positive bias.....	17
Figure 2.5: Conduction band energies under (a) small and (b) large negative bias....	18
Figure 2.8: Energy gap of $\text{In}_x\text{Ga}_{1-x}\text{As}$ as a function of indium concentration.....	18
Figure 3.1: Lattice sizes of InAs and GaAs .....	19
Figure 3.2: Lattice mismatch of InAs grown on GaAs.....	19
Figure 3.3: Cross section of QD growth (a) substrate (b) InAs growth on GaAs before critical thickness is reached (c) self assembled QDs once critical thickness is achieved .....	20

Figure 3.4: (a) Top view and (b) side view of dots taken using atomic force microscopy	22
Figure 3.5: Cross section of quantum dots taken with transmission electron microscope	22
Figure 3.6: Block diagram for photoluminescence test set up	23
Figure 3.7: Photoluminescence of a multi spectral quantum dot infrared photodetector	24
Figure 3.8: Diagram of fabrication steps to form the mesa (a) wafer before processing (b) coated with photoresist (c) photoresist patterned (c) mesa etched into wafer	25
Figure 3.9: Diagram of fabrication steps to form the electrodes on mesa (a) coated with photoresist (b) electrode pattern in photoresist (c) metal deposited on pattern (c) electrodes after liftoff	26
Figure 3.10: (a) Completed 12x12 array of photodetectors (b) magnified view showing top and bottom electrode on mesa	26
Figure 3.11: (a) Diagram of a fabricated device mounted on a copper substrate and wire bonded for testing (b) image of 4x4 array of photodetectors mounted and wire bonded for testing	27
Figure 3.12: (a) Diagram of temperature controlled dewar (b) picture of dewar	27
Figure 4.1: Block diagram of spectrum response test setup	29
Figure 4.2: Photocurrent spectrum response of a quantum dot infrared photodetector	29
Figure 4.3: Graph of dark current density	30
Figure 4.4: Block diagram of noise current test setup	31
Figure 4.5: Graph of noise current of QDIP	32
Figure 4.6: Graph of photoconductive gain	33
Figure 4.7: Block diagram of responsivity test setup	34
Figure 4.8: Graph of blackbody radiation at 1000K	35

Figure 4.9: Transmission of bandpass optical filters.....	35
Figure 4.10: Responsivity as a function of bias voltage for each band.....	37
Figure 4.11: Detectivity as a function of bias voltage for each band.....	38

## I INTRODUCTION

### 1.1 WHAT IS INFRARED LIGHT

Infrared (IR) light is defined as electromagnetic radiation between the wavelengths 0.7 and 1000  $\mu\text{m}$  [1]. All objects that are above absolute zero emit IR radiation. The amount of light that an object emits is dependent on the absolute temperature of the device and surface conditions of the object. The equation and graph below illustrate the IR radiation of a blackbody source at 1000K.

$$I(\lambda, T) = \frac{2hc^2}{\lambda^5} \frac{1}{e^{\frac{hc}{\lambda kT}} - 1} \quad (1.1)$$

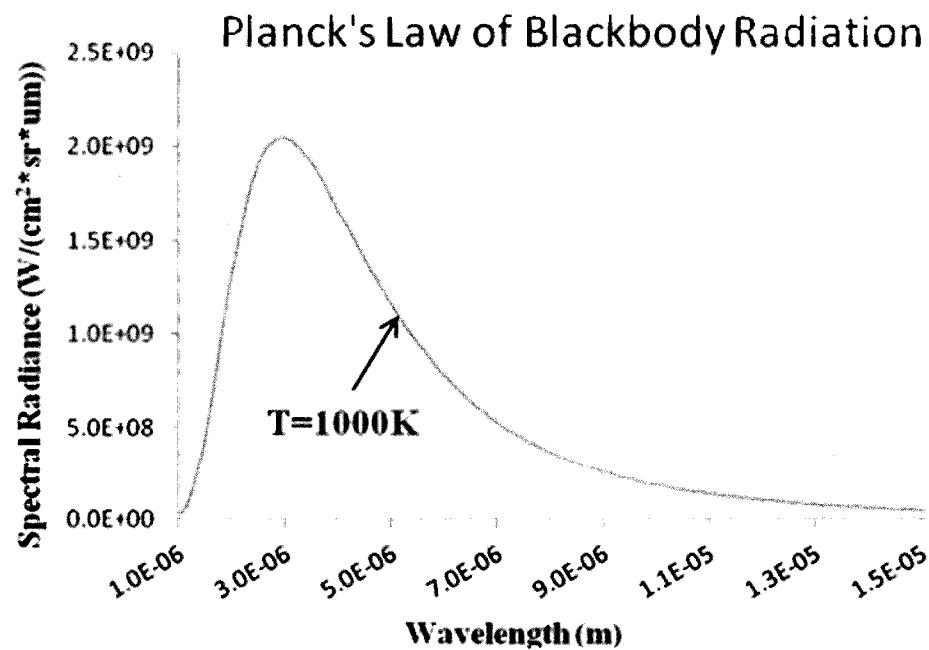


**Figure 1.1:** Spectral radiance of a blackbody source at T=1000K

Figure 1.2 shows the atmospheric transmission of the IR spectrum and the three detection bands it is divided into. The bands are shortwave infrared (SWIR) from 0.7 to 2.0 $\mu\text{m}$ , midwave infrared (MWIR) from 3 to 5 $\mu\text{m}$ , and longwave infrared (LWIR) from 8 to 14 $\mu\text{m}$  [2]. Within these bands the atmospheric absorption is at a minimum, they are sometimes referred to as atmospheric windows.

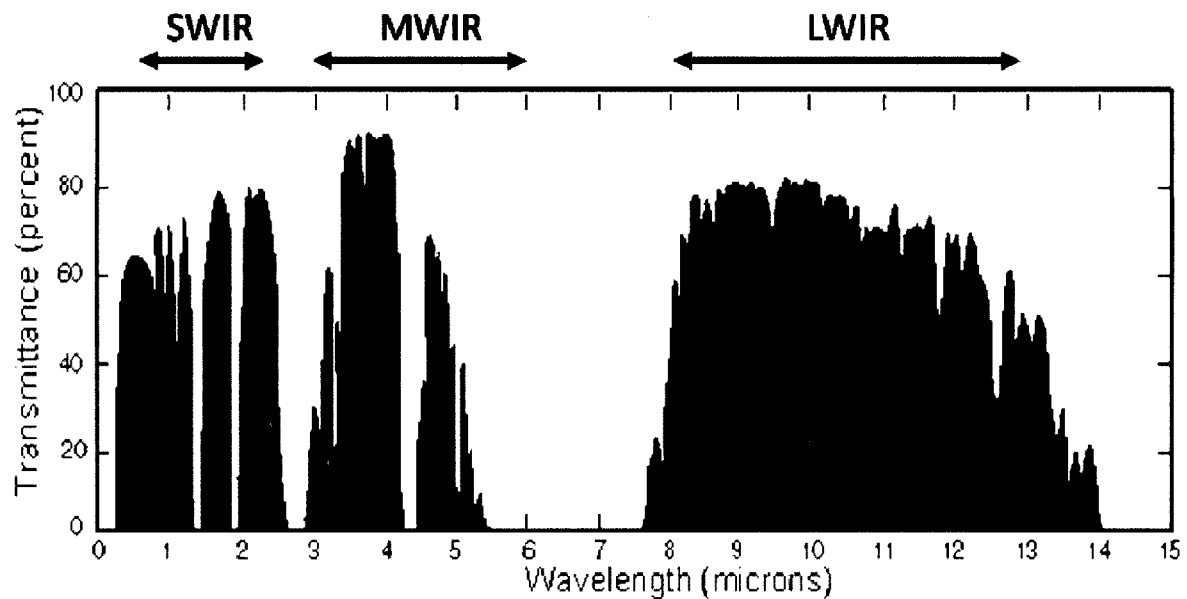


**Figure 1.2:** Atmospheric transmission of IR light

## 1.2 APPLICATIONS OF INFRARED DETECTORS

Since the human eye can only detect photons with wavelengths between  $\sim 0.4$  and  $\sim 0.7\mu\text{m}$  a large number of photons that are emitted by everyday objects are invisible. IR detectors can make the light at wavelengths outside of the visible spectrum visible. Figures 1.3 and 1.4 are comparisons of images that have been taken using visible and infrared light

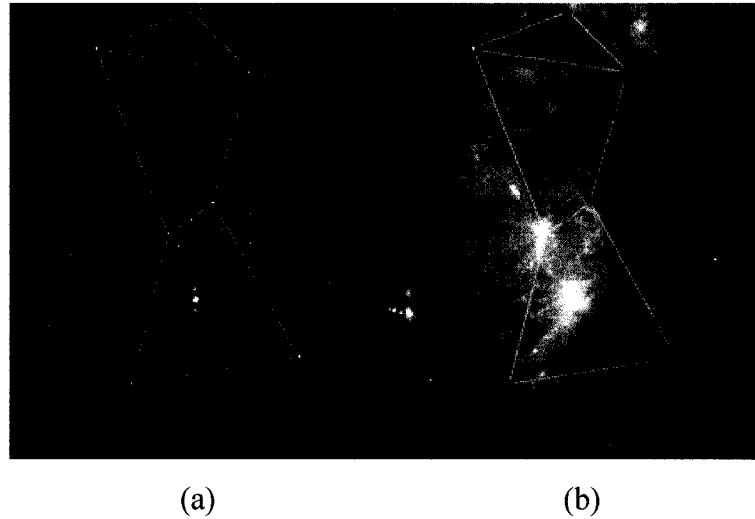


**Figure 1.3:** Comparison of a constellation using (a) visible and (b) infrared light

\*Image from [http://coolcosmos.ipac.caltech.edu/cosmic\\_kids/learn\\_sirtf/images/orion.gif](http://coolcosmos.ipac.caltech.edu/cosmic_kids/learn_sirtf/images/orion.gif)

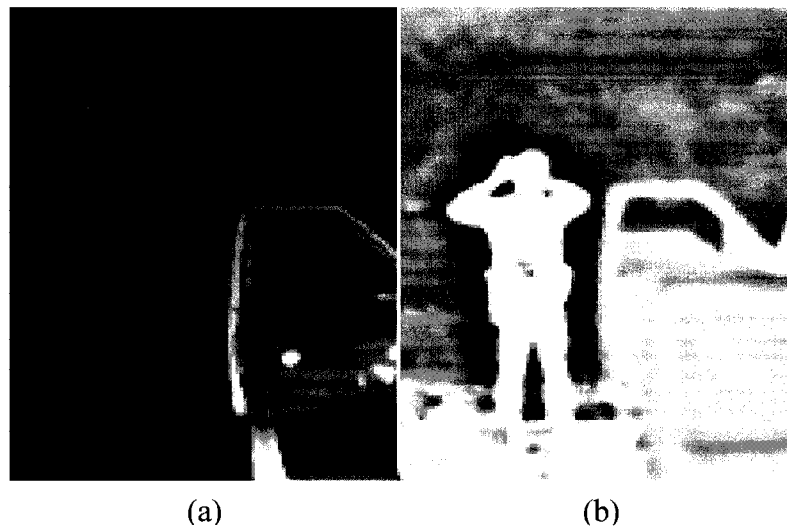


**Figure 1.4:** Comparison of (a) visible and (b) infrared images

\*Images from [www.thermal-eye.com](http://www.thermal-eye.com)

Because of their ability to provide sensing and imaging beyond the limited visible portion of the electromagnetic spectrum, IR detectors are of great important in numerous defense and civilian related applications, including temperature registration, objects discrimination and identification, remote sensing, environment monitoring, material analysis and medical diagnostics [3-7].

## 1.3 CURRENT DETECTOR TECHNOLOGIES

Infrared detectors can be divided into two general categories. The first is thermal detectors, which rely on the incident radiation to change the temperature of the detector material, thereby creating a change in the material properties that can then be detected. The second detector category is photon detectors, which rely on the energy of the photon to be absorbed by the semiconductor and that absorption will cause an electron transition to a higher energy level. The first thermal detector was invented by Herschel in 1800; it consisted of a liquid in a glass thermometer with a blackened bulb to absorb the radiation [6]. This simple detector was used to discover the existence of the infrared spectrum.

### 1.3.1 THERMAL DETECTOR TECHNOLOGIES

Since thermal detectors rely on the radiant power of the incident light and not its spectral content, thermal detectors are generally wavelength independent over a broad spectrum. Until recently, thermal detectors were considered to be slow and insensitive compared to other types of detectors. There has been considerable research over the last decade that has improved the response time, increased the sensitivity, decreased the noise and integrated the detectors into focal plane arrays. With the realization of focal plane arrays, thermal detectors have gained popularity in applications that require uncooled operation. Figure 1.5 is an illustration of a very simple thermal detector.

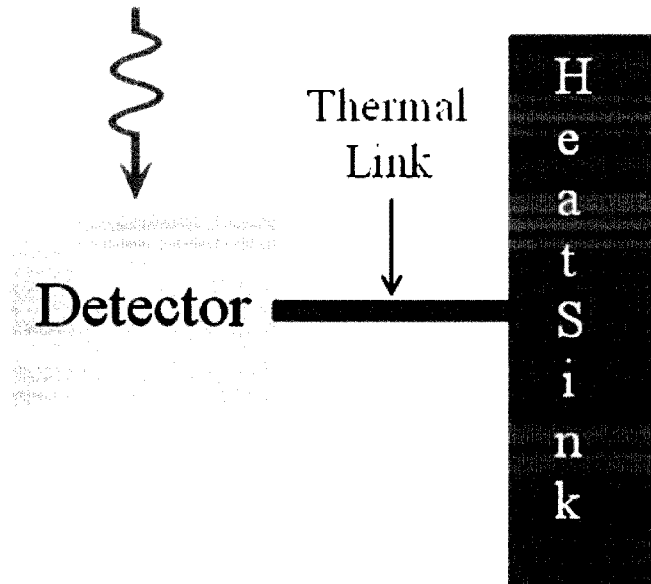


**Figure 1.5:** Diagram of a simple thermal detector

#### Thermopile:

A thermopile is essentially a junction between two dissimilar conductors. Early thermopiles were made from either a junction between copper and constantan or bismuth and silver. Modern thermopiles are made from thin films that can be fabricated into complex arrays. The response time for thermopiles is slow compared to other thermal detectors and requires specially designed amplifiers which are large and expensive. Despite the drawbacks, thermopiles are still commonly used in space instruments and ground based metrological devices[6].

#### Bolometer:

A bolometer consists of a resistive element with a large temperature coefficient so that a small change in the absorbed radiant power will cause a large change in the resistance of the element. Bolometers can be operated at room temperature or cryogenically cooled to increase performance: however, operating at cryogenic temperatures adds size, weight, and



cost to the detector design. Modern bolometers are based on semiconducting films which allows the size of the element to be significantly reduced. These smaller elements are called microbolometers and are commonly used in commercial and defense related sensing and imaging applications[6].

#### Pyroelectric:

The internal polarization of pyroelectric materials is changed as radiant energy is absorbed, causing an electric potential to develop across the crystal. When the incident radiation is constant, no change can be sensed. This requires the use of an optical chopper to modulate the light. Pyroelectric detectors have a fast response time and have a broad spectral response[6].

### 1.3.2 PHOTON DETECTOR TECHNOLOGIES

Photon detectors are characterized by a fast response time and high sensitivity, although their spectral response is dependent on wavelength. Photon detectors can be divided into many subcategories. For the purposes of this paper they will be divided into two categories; detectors, that are based on interband transitions and, detectors based on intersubband transitions.

#### Interband Transition:

An interband transition occurs when a photon of sufficient energy is absorbed by the photodetector material causing an electron to transition from its bound state in the valence band to a higher energy in the conduction band where it is free to contribute to photocurrent.

Figure 1.6 illustrates the photon on energy  $h\nu$  being absorbed and causing the electron to transition to the conduction band.

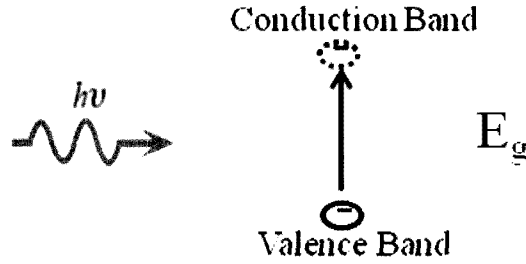


**Figure 1.6:** Diagram of photon absorption in a semiconductor

The condition for the electron to be absorbed by the semiconductor and cause the electron to transition from the valence band to a higher energy in the conduction band is shown below.

$$E_{ph} \geq E_g \quad (1.2)$$

The energy gap  $E_g$  is a material dependent property and the energy of the photon  $E_{ph}$  is given by the equation:

$$E_{ph} = h\nu = \frac{hc}{\lambda} \quad (1.3)$$

Where  $h$  is planks constant,  $c$  is the speed of light in vacuum, and  $\lambda$  is wavelength.

The challenge of creating an infrared detector based on an interband transition lies in the low energy of the photons at long wavelengths. Figure 1.7 is a plot of the energy of the photon as a function of wavelength. From the Figure 1.7, the necessary energy gap for a photon with a wavelength of 10 microns is 0.124eV. Table 1.1 shows some common semiconductors and the range of energy gaps. The only available semiconductor alloy whose

energy gap is low enough to absorb a photon with energy of 0.124eV is mercury cadmium telluride ( $\text{Hg}_{1-x}\text{Cd}_x\text{Te}$ ).

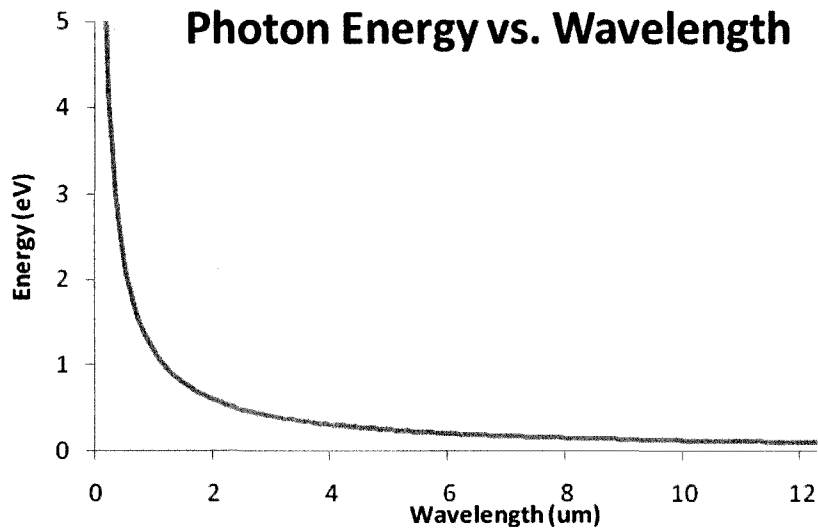


**Figure 1.7:** Graph of photon energy versus wavelength

**Table 1.1:** Energy gap of common semiconductors.

Semiconductor	Energy Gap (eV)
Si	1.12
Ge	0.66
GaAs	1.42
$\text{Al}_x\text{Ga}_{1-x}\text{As}$	1.42-1.93
$\text{In}_{1-x}\text{Ga}_x\text{As}$	0.75-1.42
$\text{In}_{1-x}\text{Ga}_x\text{As}_y\text{P}_{1-y}$	0.78-1.24
InP	1.35
InSb	0.25-1.24
$\text{Hg}_{1-x}\text{Cd}_x\text{Te}$	0.03-1.5

### Mercury Cadmium Telluride (MCT):

Mercury cadmium telluride is a narrow band gap ternary semiconductor alloy that is suitable for use in LWIR photodetectors. The band gap energy MCT of varies as a function of cadmium and absolute temperature. The equation which describes this relationship is given by:

$$E_g (eV) = 1.59x - 0.25 + 5.233(10^{-4})(T)(1 - 2.08x) + 0.327x^3 \quad (1.4)$$

Where  $x$  is the fraction of cadmium and  $T$  is the absolute temperature [11].

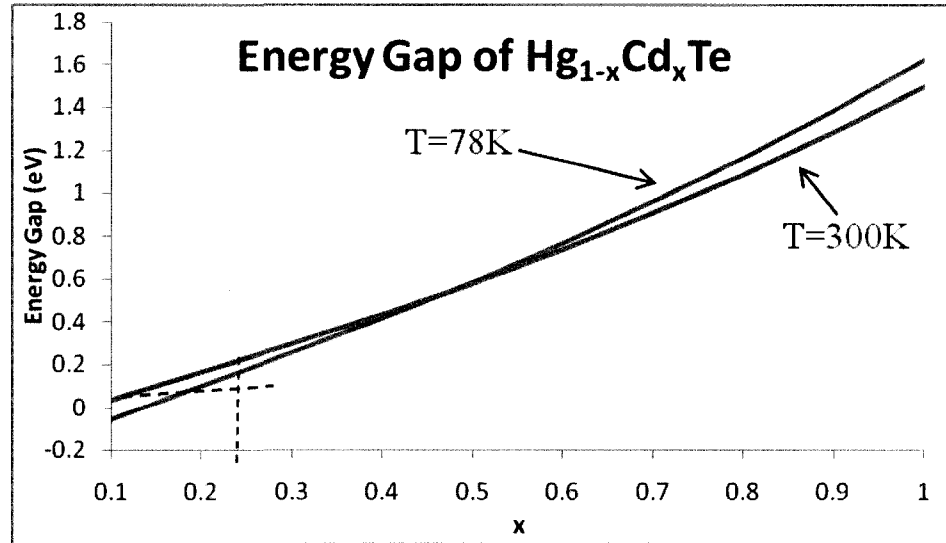


**Figure 1.8:** Graph of energy gap of HgCdTe as a function of cadmium content

Current of state-of-the-art infrared detection and sensing technology is based on the MCT material systems. However, the MCT technology still has several issues, including difficulties in material growth, high cost, and an operating temperature  $< 80$  K to avoid Auger recombination process [9], which reduces the photo-excited carrier lifetime and leads to low carrier collecting efficiency and low quantum efficiency [9, 10]

## Auger Recombination:

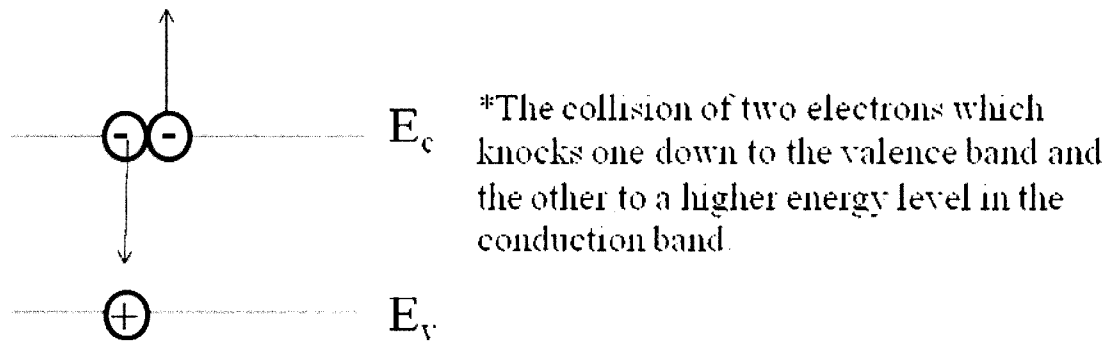


**Figure 1.9:** Diagram of Auger recombination mechanism

## Intersubband transitions:

Intersubband transitions are electrons that transition from one energy level in the conduction band to a higher energy level within the conduction band. The figure below illustrates the electron transition within the conduction band.

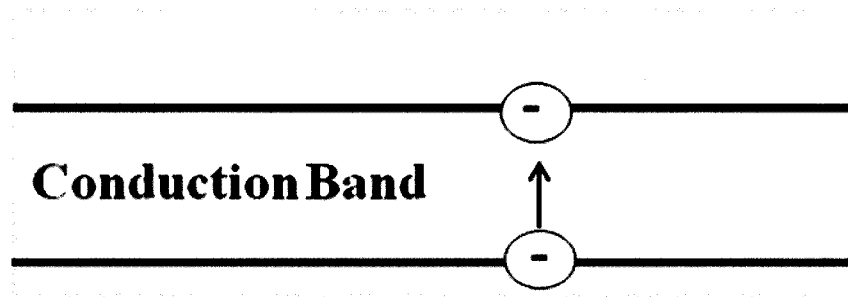


**Figure 1.10:** Simplified diagram of intersubband transition

The energy level separation within the conduction band arises from quantum confinement. A more detailed analysis on the separation of energy levels in the conduction band will be discussed in section II. The first practical device to exploit intersubband transitions was the quantum well infrared photodetector (QWIP). A QWIP is a detector

consisting of a thin layer of a lower energy gap material sandwiched between thick layers of a higher band gap material. A simple QWIP structure is shown below.

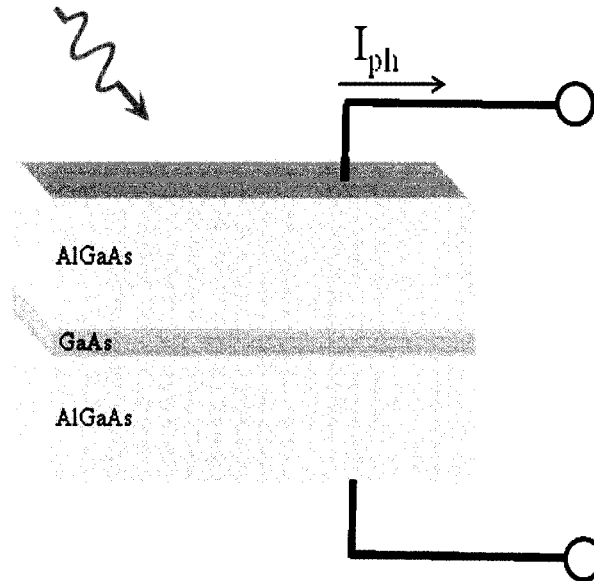


**Figure 1.11:** Diagram of a quantum well infrared photodetector

The basic principle operation is the incident light of sufficient energy, is absorbed by the QWIP causing the electron to transition to a higher energy level in the conduction band. The applied bias causes the electron to tunnel through the potential barrier to the continuum where it can be collected as photocurrent.

The major drawback of the QWIP technology is its inability to absorb normally incidence radiation due to the polarization selection rules [12, 14]. This problem can be solved by using surface grating structures to couple normal incidence to side incidence [14]. However, this approach adds cost and fabrication complexity.

### Quantum dot infrared photodetectors (QDIP)

A QDIP is similar to a QWIP except that it has been spatially confined in three dimensions (3-D), whereas a QWIP has been confined in one dimension. These small nanostructures are called quantum dots (QD). QDIPs based on intersubband transitions in self-assembled InAs QD have emerged as a promising technology for MWIR and LWIR sensing and imaging [3-8]. The advantages provided by the 3-D quantum confined QD heterostructure include: intrinsic sensitivity to normal incident radiation [6-8], possibility of lower dark current density [7, 8], and long excited state lifetime due to the reduced electron-phonon scattering [9]. The long excited state lifetime not only allows efficient collection of photo-excited carriers, but also leads to high photoconductive gain and photoresponsivity [11]. By enhancing the photoresponsivity and lowering the noise levels, the QDIP technology is believed to be promising for high temperature operation [13-14].

## II PHYSICS OF OPERATION

### 2.1 INTERBAND vs. INTERSUBBAND TRANSITIONS

To better understand intersubband transitions a brief review of interband transitions will be given for comparison. In a bulk semiconductor the energy levels in the conduction are considered to be continuous. However, a more accurate description of the energy levels would be to say there are a large number of closely spaced, discrete energy levels. The inset in figure 2.1(b) shows the discrete energy levels in the conduction band.

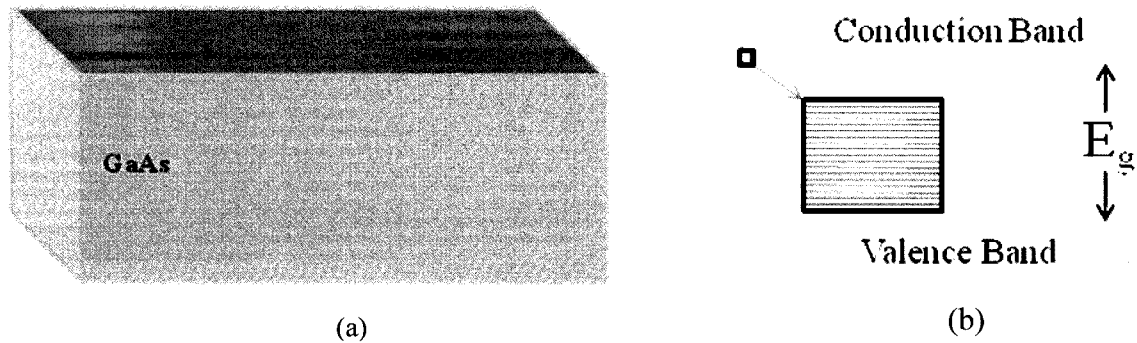


**Figure 2.1:** (a) Bulk GaAs and (b) energy band diagram for bulk GaAs showing the closely spaced energy levels in conduction band

Through quantum confinement, the difference in the energy levels will increase which gives rise to the discrete energy levels described by equation 2.1. Figure 2.2(a) shows the one dimensional confinement of a quantum well.



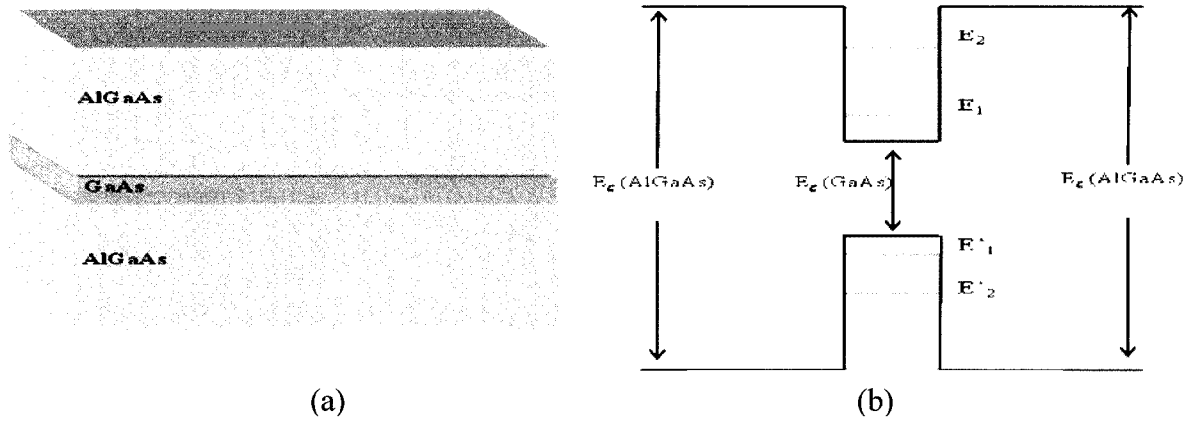


**Figure 2.2:** (a) Quantum well structure and (b) energy levels

$$E_n = \frac{\hbar^2 \pi^2}{2m^* d^2} n^2 \quad (2.1)$$

Where  $\hbar$  is Planck's constant reduced,  $m^*$  is effective mass of either the electron or hole in the conduction band or valence band respectively. The thickness of the well is  $d$  and  $n$  is the integer number of the discrete energy level. When there is the structure is quantization in all three spatial dimensions the discrete energy levels can be described by equation 2.2.

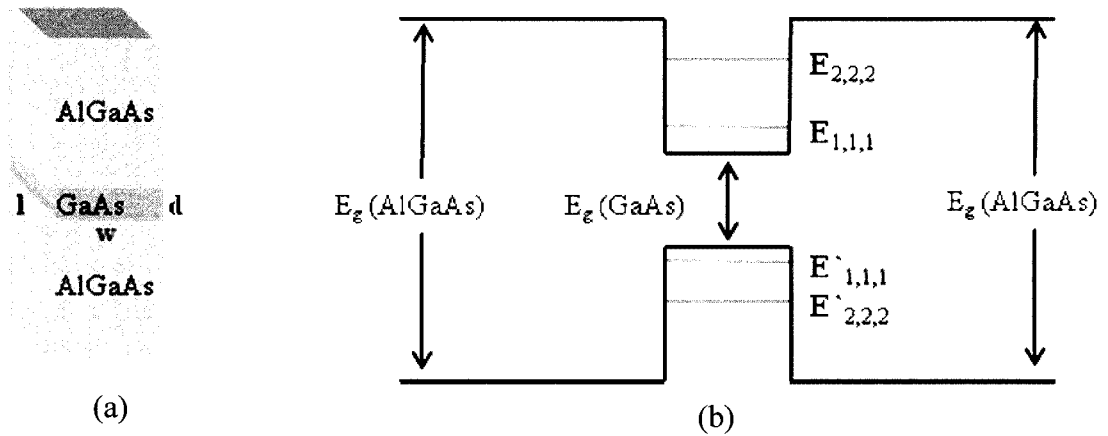


**Figure 2.3:** (a) Structure of quantum dot and (b) energy levels

$$E_{n,m,p} = \frac{\hbar^2 \pi^2}{2m^*} \left( \frac{n^2}{d^2} + \frac{m^2}{l^2} + \frac{p^2}{w^2} \right) \quad (2.2)$$

## 2.2 MULTISPECTRAL OPERATION

There have been a few reported multispectral QDIPs [24-27]. Most of these multi incorporate QDs with different sizes or rely on different energy levels of the QDs. For conventional MBE growth, the size of the QDs depends on several different growth parameters such as substrate temperature, growth rate, and material flow rate, which make the QD size tuning quite complicated and usually non-repeatable. An improved design relies on vertically-stacked InAs quantum dot layers of consistent size with two different capping layers, i.e. (GaAs and  $\text{In}_{0.15}\text{Ga}_{0.85}\text{As}$ ). Using GaAs as a capping layer will form a symmetric potential well. The size of the dot can be engineered to absorb the shorter wavelength of light. By using the InGaAs as a capping layer and varying the indium concentration and the thickness of the InGaAs capping layer the energy levels of the QD will decrease providing the absorption of the longer wavelength. Figures 2.4 and 2.5 show the effect of the magnitude of the bias voltage on the conduction band.

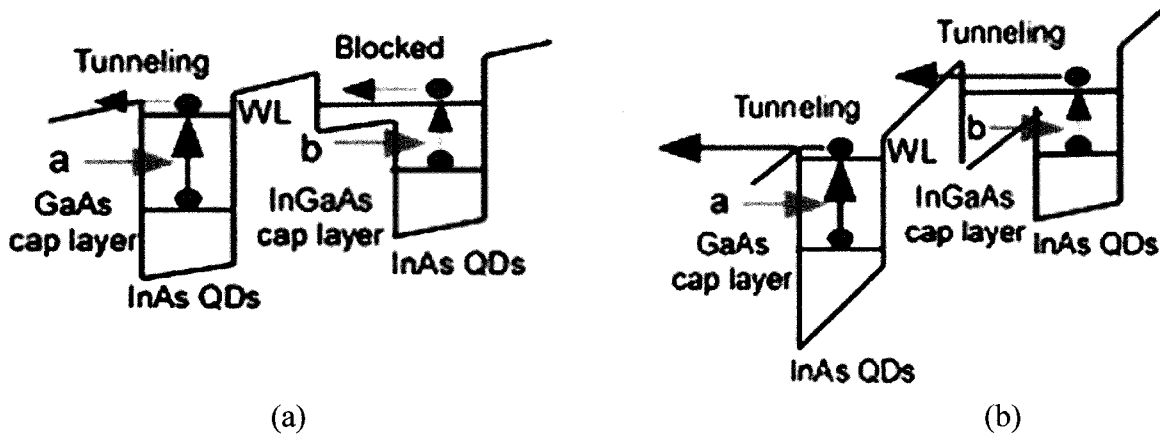


**Figure 2.4:** Conduction band energies under (a) less reverse bias (b) more reverse bias

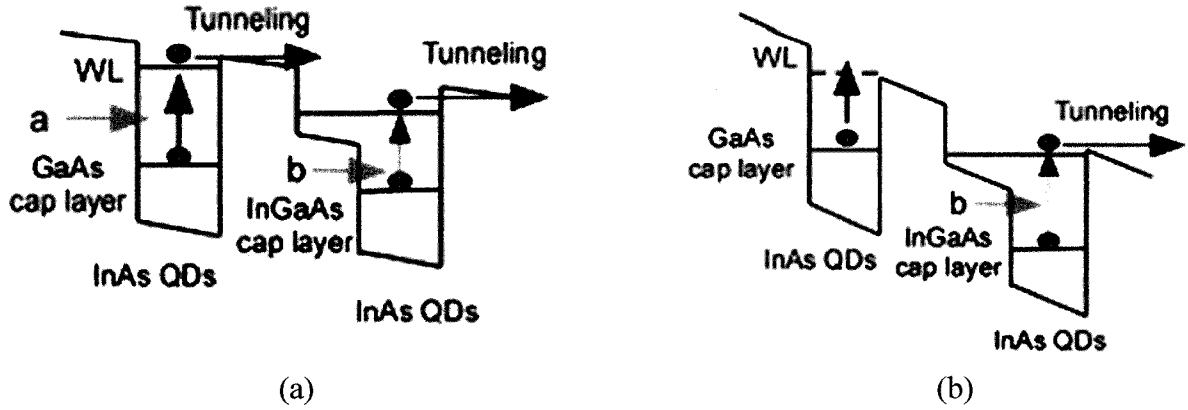


**Figure 2.5:** Conduction band energies under (a) less forward bias (b) more forward bias

The energy level of InGaAs can be tuned by varying the concentration of indium, the equation that governs the energy gap is shown below.

$$E_g(x) = 1.425 - 1.501x + 0.436x^2 \quad (2.4)$$

Figure 2.8 is a graph of equation 2.4.

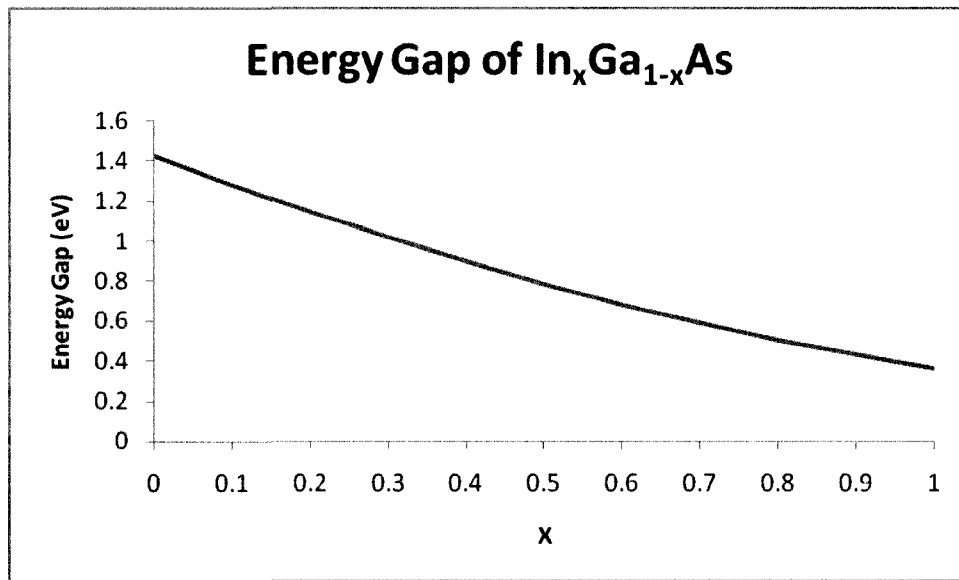


**Figure 2.8:** Energy gap of  $\text{In}_x\text{Ga}_{1-x}\text{As}$  as a function of indium concentration

### III GROWTH and FABRICATON

#### 3.1 MOLECULAR BEAM EPITAXY GROWTH

Molecular beam epitaxy (MBE) was chosen as the growth method for the multispectral QDIP. With MBE growths it is possible to grow high quality atomic layer films. The self assembled quantum dots were grown by the Stranski-Krastanow (SK) method. The SK method of growing quantum dots consists of growing a lattice mismatched film of InAs on GaAs. This lattice mismatch is illustrated in the figure below.

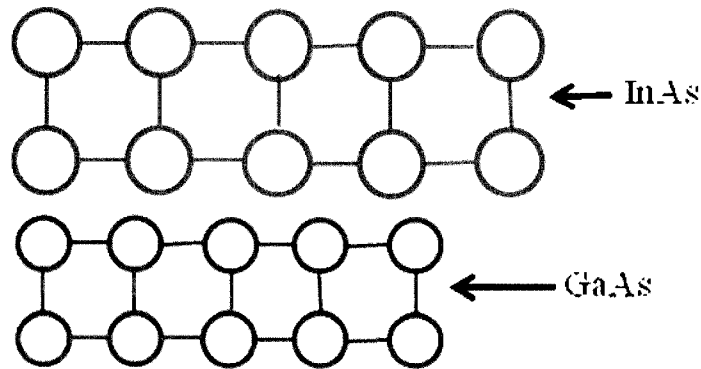


**Figure 3.1:** Lattice sizes of InAs and GaAs

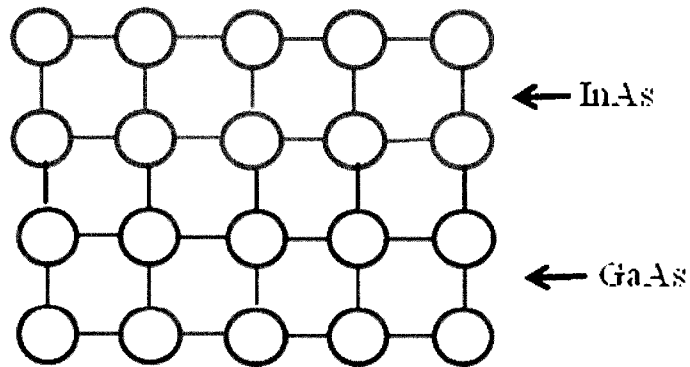


**Figure 3.2:** Lattice mismatch of InAs grown on GaAs

When the film reaches a critical thickness the stress in the film is the great and the quantum dots are formed to relax the stress. Figure 3.3 (a) shows the substrate on which the self assembled dots will be grown (b) shows the GaAs layer that has been grown and the lattice mismatched film of InAs that is being grown before the critical thickness is reached. Figure 3.3 (c) shows the islands that have spontaneously formed to relax the stress that has accumulated in the film.

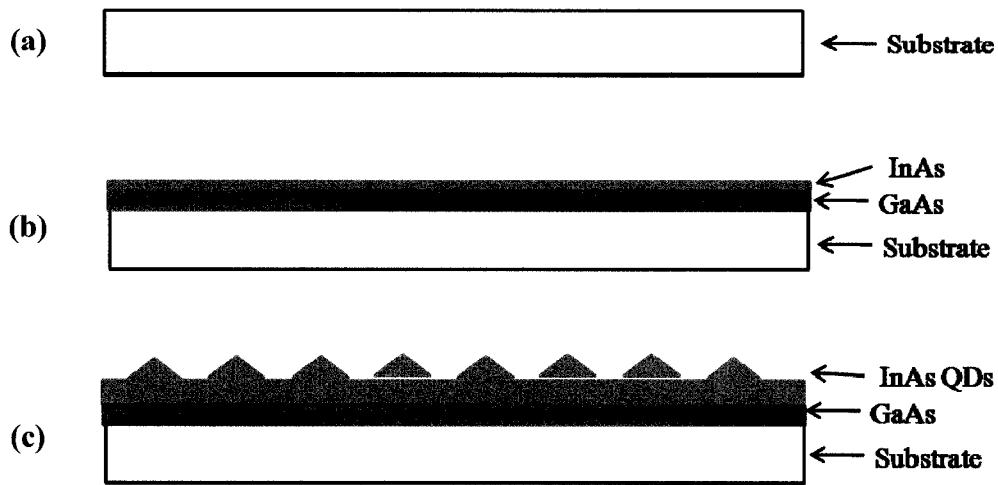


**Figure 3.3:** Cross section of QD growth (a) substrate (b) InAs growth on GaAs before critical thickness is reached (c) self assembled QDs once critical thickness is achieved

### 3.2 GROWTH CONDITIONS

The multispectral QDIP consists of vertically stacked QD layers with GaAs and  $\text{In}_{0.15}\text{Ga}_{0.85}\text{As}$  capping layers for NLWIR and LWIR band absorption, respectively. Each of the QD absorption band consists of 10-period of InAs QD layers with the corresponding capping layers. The QD layer is then sandwiched between the bottom and top GaAs contact layers. The QDIP was grown using a V80H MBE System. A  $0.3\mu\text{m}$  Si-doped (n+) GaAs bottom contact layer ( $n = 1 \times 10^{18} \text{ cm}^{-3}$ ) was first grown on a semi-insulating GaAs (100)

wafer, followed by the growth of a 60 nm undoped GaAs buffer layer. The growth temperature for the GaAs contact and buffer layers was set to 620 °C. The LWIR and MWIR QD absorption regions were then grown. The LWIR and NLWIR QD regions consist of ten periods of three monolayers (ML) of InAs QDs with 20 ML  $\text{In}_{0.15}\text{Ga}_{0.85}\text{As}$  and 45 nm GaAs cap layers, respectively. 50 nm GaAs spacer layers were grown between the QD layers. The growth rates of the InAs QDs, the  $\text{In}_{0.15}\text{Ga}_{0.85}\text{As}$  cap and the GaAs spacer were 0.16, 0.8, and 0.9 ML/s, respectively. The doping level of the QD region was estimated to be  $3.5 \times 10^{17} \text{ cm}^{-3}$ . The QD layers and cap layers were grown at 470 °C. The QD active layer was then covered by a 20 nm undoped  $\text{Al}_{0.30}\text{Ga}_{0.70}\text{As}$  top current-blocking layer and 0.1  $\mu\text{m}$  highly Si-doped ( $n=1 \times 10^{18} \text{ cm}^{-3}$ ) GaAs contact layer. Figure 3.4 shows atomic force microscopy images of the dots. From these images the dots density is estimated to be  $2.9 \times 10^{10} \text{ cm}^{-2}$ . Figure 3.5 shows a cross section of the quantum dots taken with transmission electron microscopy. The size of the quantum dots are estimated to be ~6nm high and ~25nm high.

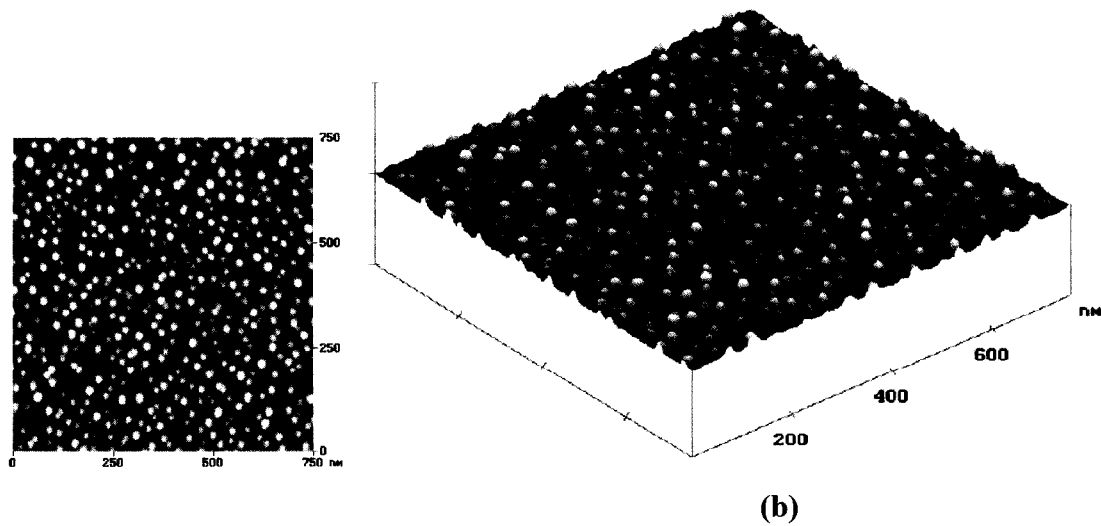


**Figure 3.4:** (a) Top view and (b) side view of quantum dots taken using atomic force



**Figure 3.5:** Cross section of quantum dots taken with transmission electron microscope

### 3.3 PHOTOLUMINESCENCE

Photoluminescence (PL) spectroscopy is a simple and effective method for determining the energy levels of the quantum dot structures. A PL measurement is generally taken after the MBE growth and before any fabrication begins to determine if the MBE growth was successful.

The PL of the QDIP sample was measured at room temperature (RT) using a continuous wave argon ( $\text{Ar}^{3+}$ ) laser with excitation wavelength of 514nm and a laser output power of 300mW. The laser spot size was measured to be  $\sim 0.5\text{mm}^2$ . Figure 3.6 shows a block diagram of the test setup for PL measurements.

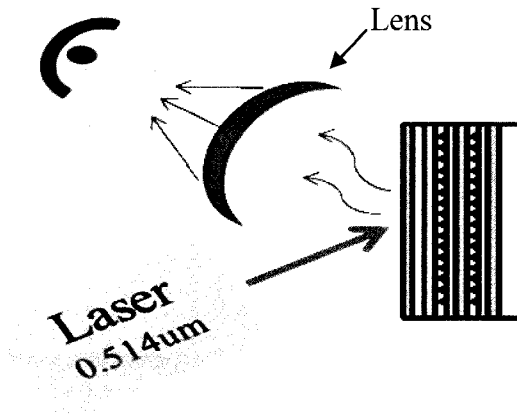


**Figure 3.6:** Block diagram for photoluminescence test set up

The laser will excite electrons to a higher level in the conduction band and through spontaneous emission they will relax back to the valence band. This spontaneous emission will be focused by the lens on the photodetector for detection.

Figure 3.7 shows the PL spectrum at the sample temperature of 4 K. The lower energy peak (1.214 eV) of the PL corresponds to the transition of the QDs with InGaAs capping layers and the higher energy peak (1.305 eV) corresponds to that of the QDs with GaAs capping layers. Note that the PL intensities are almost the same for QDs with different capping layers, which indicates the QD densities are similar for QDs with different capping layers. The slightly smaller spectrum width (FWHM) of the lower energy transition indicates better QD size uniformity with the InGaAs capping layer.



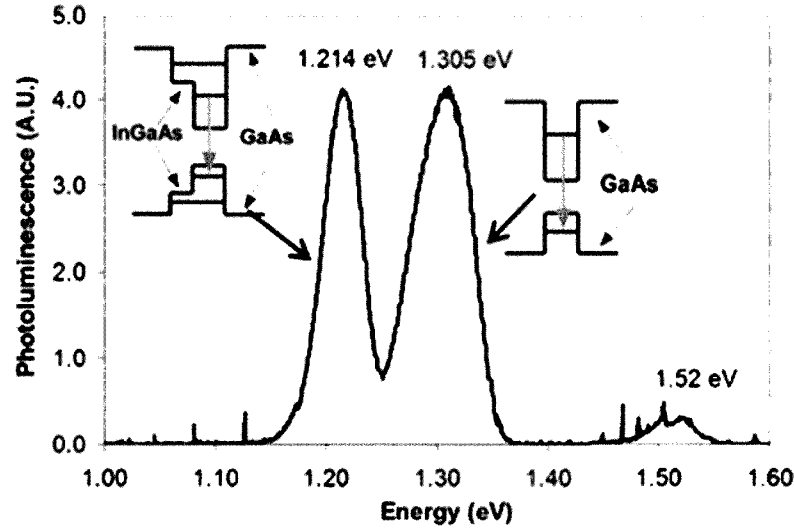


**Figure 3.7:** Photoluminescence of a multi spectral quantum dot infrared photodetector

### 3.3 FABRICATION PROCEDURE

After the growth, the wafer was processed into 100 $\mu$ m-diameter circular mesas using standard photo-lithography and wet etching procedures. The first step is to spin-coat Microposit S1822 photoresist and spin at 4000 RPM for 40 seconds. Then soft bake the sample on a hot plate at 95°C for three minutes to evaporate the coating solvent. The typical photoresist thickness was 2.6-2.8  $\mu$ m. The mesa pattern was defined by aligning a photolithography mask over the sample and exposing to ultraviolet light at a power of 25mW/cm<sup>2</sup> for nine seconds. The pattern was then developed in Microposit CD-30 developer for one minute, rinsed in deionized water, and dried with nitrogen. The sample was then immersed into a sulfuric acid solution to etch the mesa pattern. The typical etch rate was 0.5 $\mu$ m/min. Once the desired thickness was reached the photoresist was removed with acetone. The process to define the mesas is illustrated below.

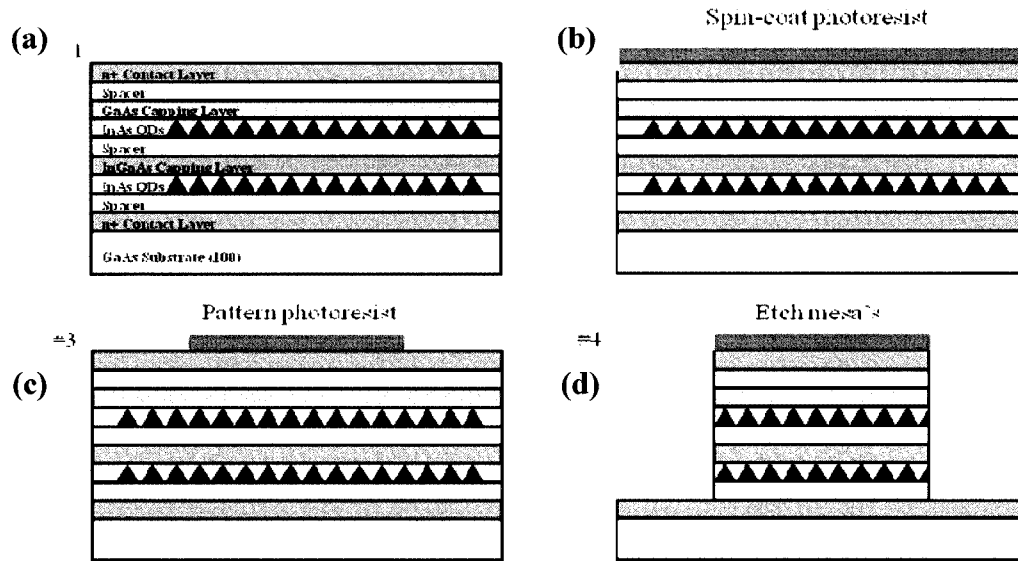


**Figure 3.8:** Diagram of fabrication steps to form the mesa (a) wafer before processing The (b) coated with photoresist (c) photoresist patterned (c) mesa etched into wafer using the same parameters as the photoresist for patterning mesas. The metal was deposited using an electron beam evaporator. A 50Å thick layer of Nickel was first deposited, followed by 170Å of Ge, 330Å of Gold, 150Å of Nickel, and then 4000Å of Gold. The samples were then annealed to form good ohmic contacts. Figure 3.9 illustrated the procedure for patterning the electrodes on the mesas and Figure 3.10

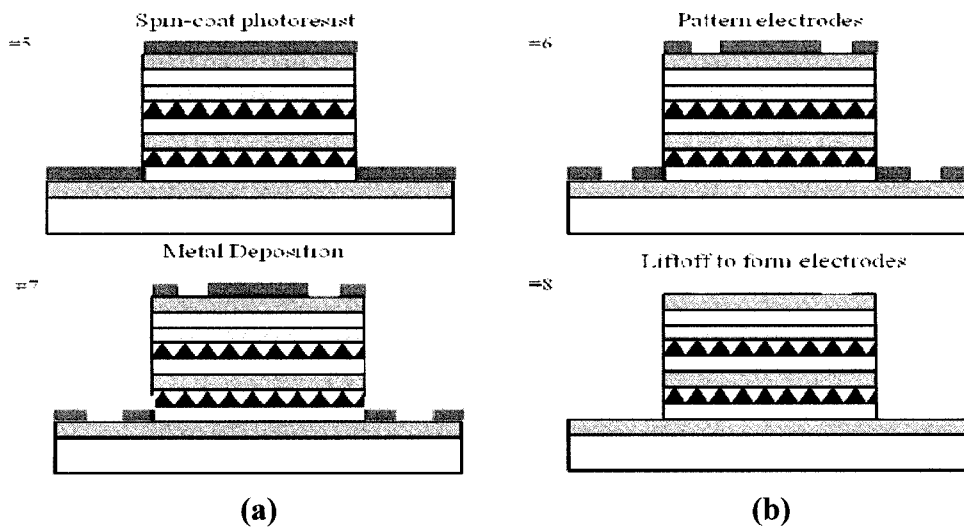




**Figure 3.10:** (a) Completed 12x12 array of photodetectors (b) magnified view showing top and bottom electrode on mesa

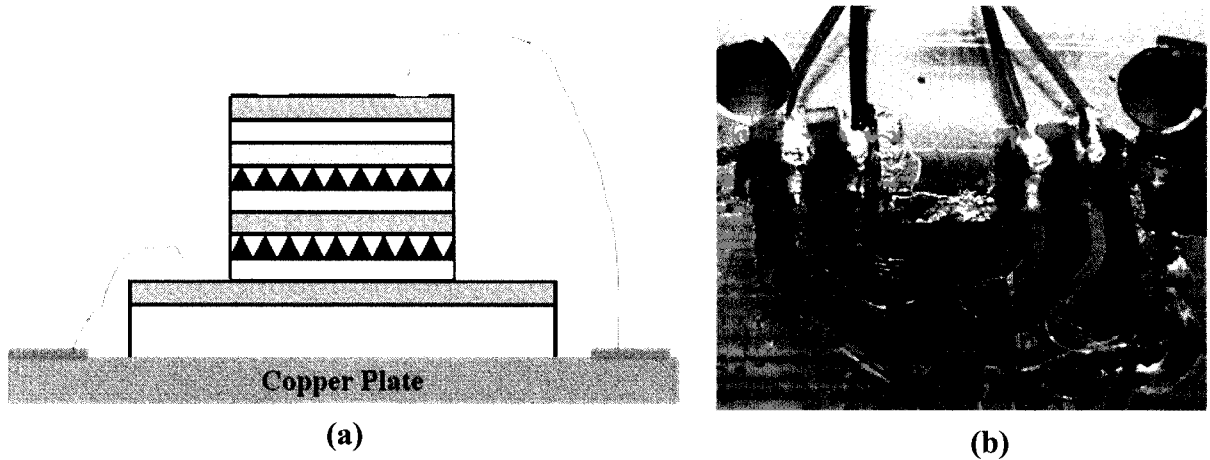


**Figure 3.11:** (a) Diagram of a fabricated device mounted on a copper substrate and wire bonded for testing (b) image of 4x4 array of photodetectors mounted and wire bonded for testing

The fabricated array of QDIPs was then wire-bonded and mounted on a cold finger inside a temperature-controlled infrared (IR) dewar with a zinc selenide (ZnSe) IR window that has more than 60% transmittance over a broad-band (3-14 μm) wavelength region.

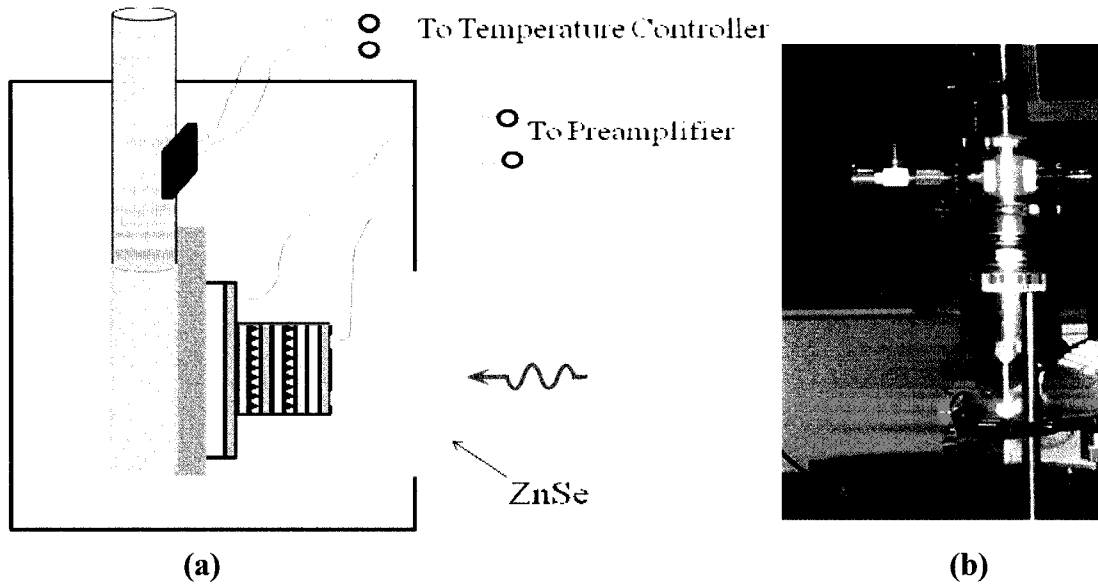


**Figure 3.12:** (a) Diagram of temperature controlled dewar (b) picture of dewar

#### 4.1 PHOTOCURRENT SPECTRUM

The spectral response of the QDIP at normal incidence was measured using a Bruker Optics Tensor27 Fourier transform infrared (FTIR) spectrometer. Figure 3(a) through figure 3(d) show the photocurrent spectrum of the QDIP at different biases at the QDIP temperature of 78K. The corresponding conduction band diagrams are shown in the inset of each figure. At the positive bias of +0.5V, the short wavelength (7.8  $\mu\text{m}$ ) photocurrents were effectively collected and the longer wavelength (10.0  $\mu\text{m}$ ) photocurrents were blocked by the barrier. When the bias voltage was increased to +0.8V, the photo-excited electrons from the LWIR absorption region can overcome the barriers and the LWIR photocurrents were effectively collected as expected. On the other hand, at a negative bias of -0.3V, since there is no barrier to block the longer wavelength (9.97  $\mu\text{m}$ ) photocurrents, both wavelength bands were detected. At bias voltage of -0.8V, only the LWIR spectrum (9.95  $\mu\text{m}$ ) showed

up. This might be because of the spreading of the wetting layer (WL) wave function, which reduces the overlap integral of the QD ground states and the WL wave functions resulting in decreased transition probability [27].

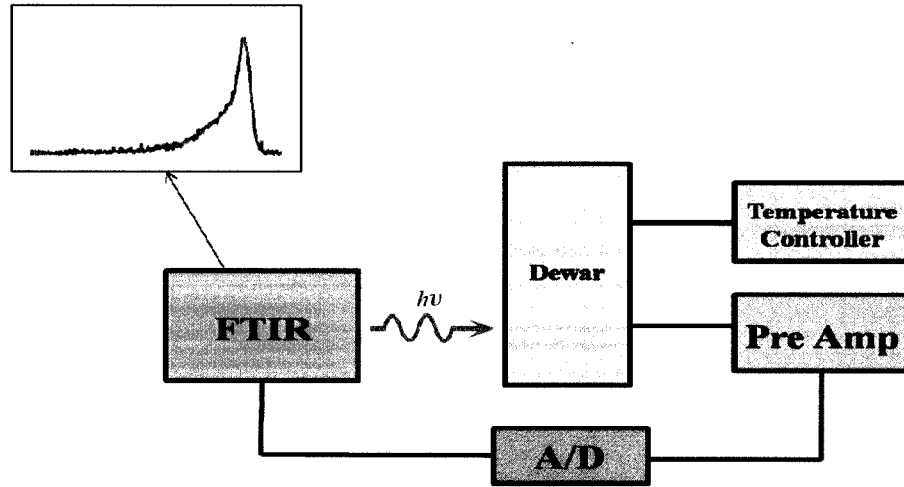


**Figure 4.1:** Block diagram of spectrum response test setup

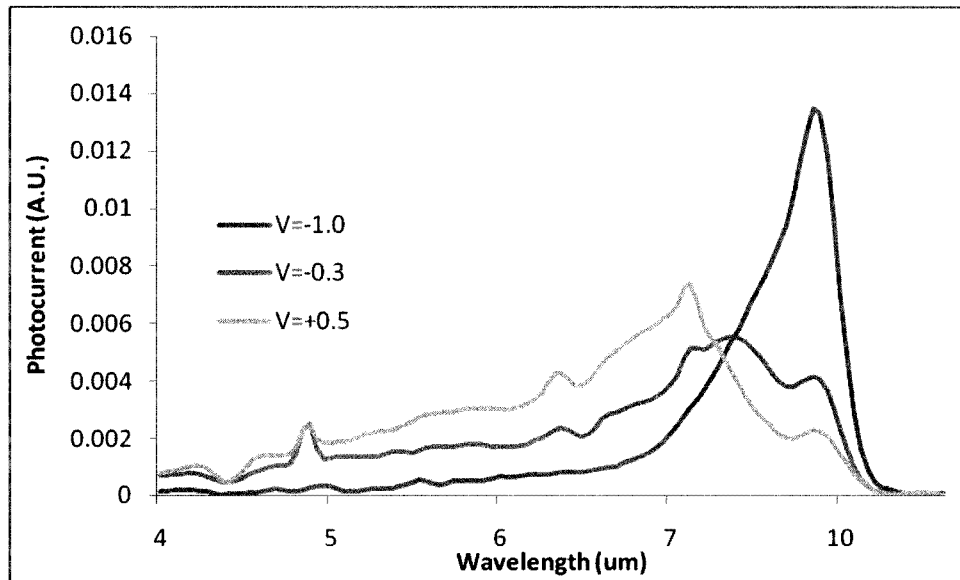


**Figure 4.2:** Spectrum response of QDIP

## 4.2 DARK CURRENT AND DARK CURRENT DENSITY

The dark current ( $I_{dark}$ ) of the QDIP was measured using an HP 4145A semiconductor parameter analyzer.

The dark current density of the QDIP can be calculated by:

$$J_{dark} = \frac{I_{dark}}{A} \quad (4.1)$$

The dark current of the QDIP at 78K and 100K is shown below in Figure 4.3.

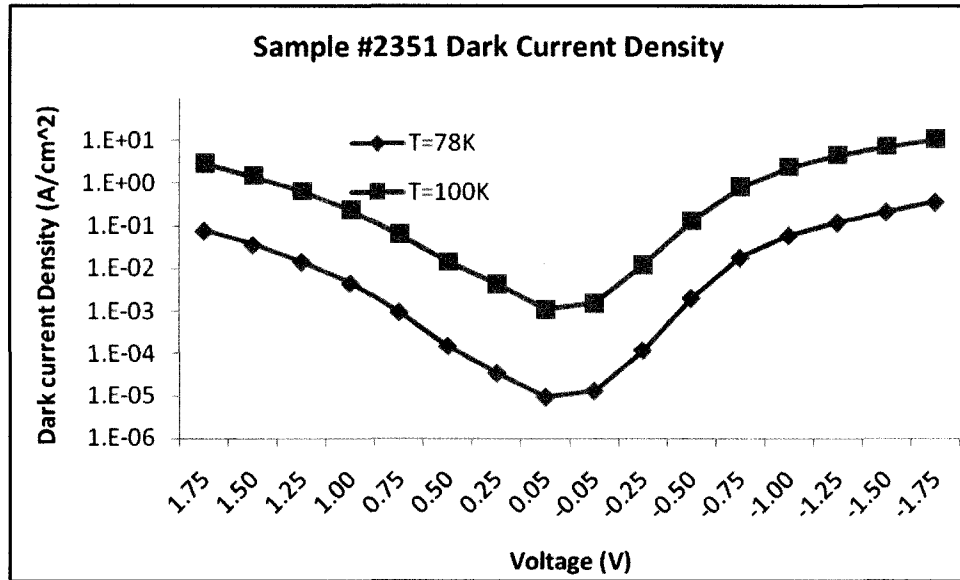


**Figure 4.3:** Graph of dark current density

### 4.3 NOISE CURRENT

The noise current ( $i_{noise}$ , in  $A/Hz^{1/2}$ ) was characterized using a Stanford Research Systems SR570 low-noise current preamplifier and a Stanford Research Systems SR760 fast Fourier transform (FFT) spectrum analyzer. To avoid  $1/f$  noise, the noise current ( $i_{noise}$ ) at 1 kHz was used for generation-recombination (GR) noise analysis [20].

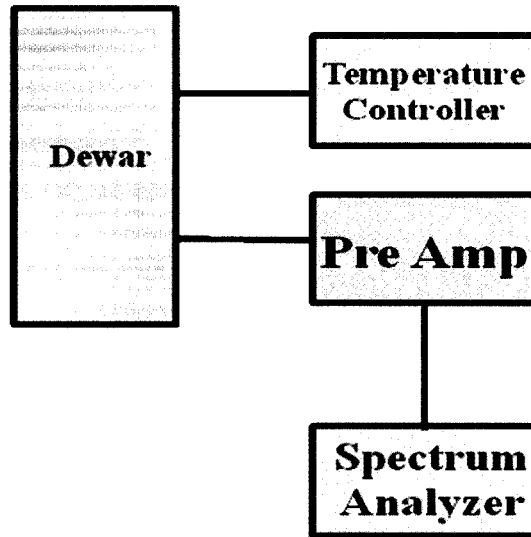


**Figure 4.4:** Block diagram of noise current test setup

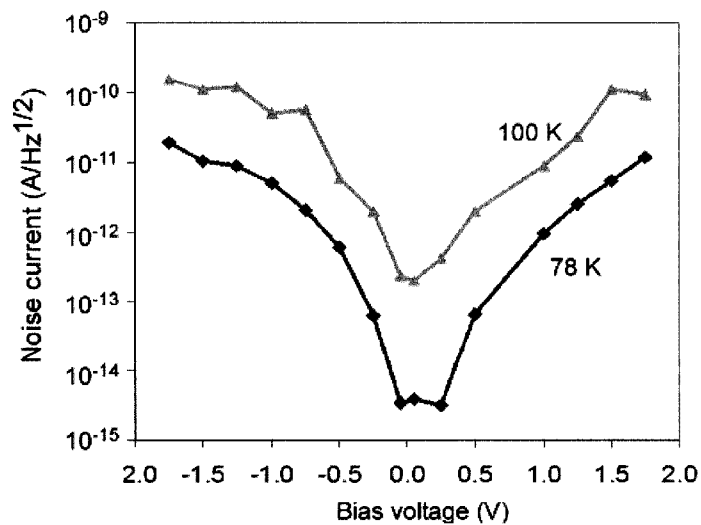


**Figure 4.5:** Graph of noise current of QDIP

Figure 4.5 shows the noise current of the QDIP as the function of biases for different temperatures. At 78 K, the noise current increases from  $3.8 \times 10^{-15} \text{ A/Hz}^{1/2}$  to  $1.2 \times 10^{-11} \text{ A/Hz}^{1/2}$  as the bias increases from 0.05 to 1.75V. At 100 K, the noise currents were measured to be  $2.0 \times 10^{-13} \text{ A/Hz}^{1/2}$  and  $9.5 \times 10^{-11} \text{ A/Hz}^{1/2}$  at the bias of 0.05 and 1.75 V, respectively.

#### 4.4 PHOTOCONDUCTIVE GAIN

As a good approximation, when the electron capture probability into a QD is small [15], the photoconductive gain and the noise gain are equal in a conventional photoconductor. The photoconductive gain can thus be calculated using [15]:

$$G = i_{\text{noise}}^2 / 4eI_d, \quad (4.1)$$

Where,  $e$  is the charge of an electron ( $1.6 \times 10^{-19} \text{ C}$ ). Figure 4.6 shows the photoconductive gain as a function of applied bias.

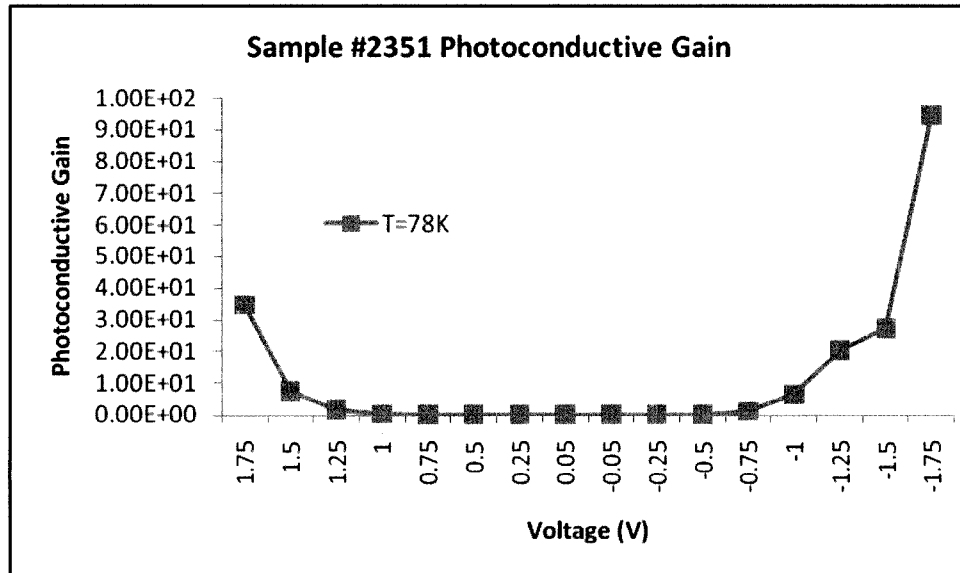


**Figure 4.6:** Graph of photoconductive gain



#### 4.5 RESPONSIVITY

Photoresponsivity is a measure of photocurrent generated per watt of incident optical energy. A block diagram of the test setup to measure the photoresponsivity of the QDIP is shown in below Figure 4.7.

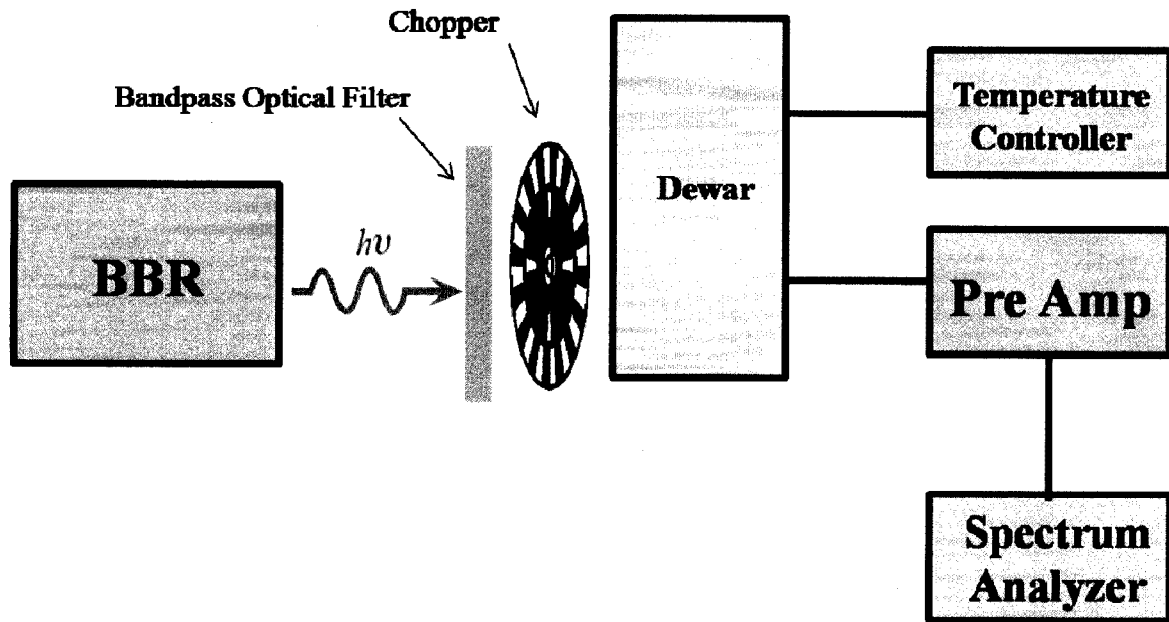


**Figure 4.7:** Block diagram of responsivity test setup

The infrared energy emitted from the blackbody source as a function of wavelength is described by:

$$I(\lambda, T) = \frac{2hc^2}{\lambda^5} \frac{1}{e^{hc/\lambda kT} - 1} \quad (4.3)$$

Where  $h$  is Planck's constant,  $c$  is the speed of light,  $k$  is Boltzmann's constant,  $T$  is the absolute temperature of the blackbody source, and  $\lambda$  is the wavelength. Figure 4.8 is a plot of the energy as a function of wavelength as a blackbody temperature of 1000K.

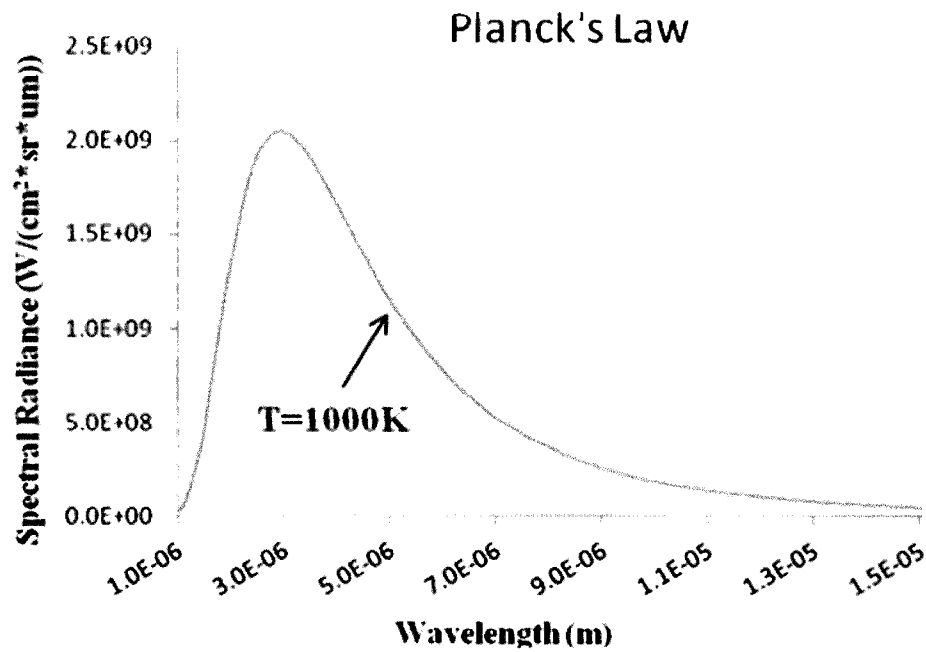


**Figure 4.8:** Graph of blackbody radiation at 1000K

A bandpass optical filter is used to provide accurate calculations of the responsivity of each detection band. The transmission of each filter is shown in the figure below.

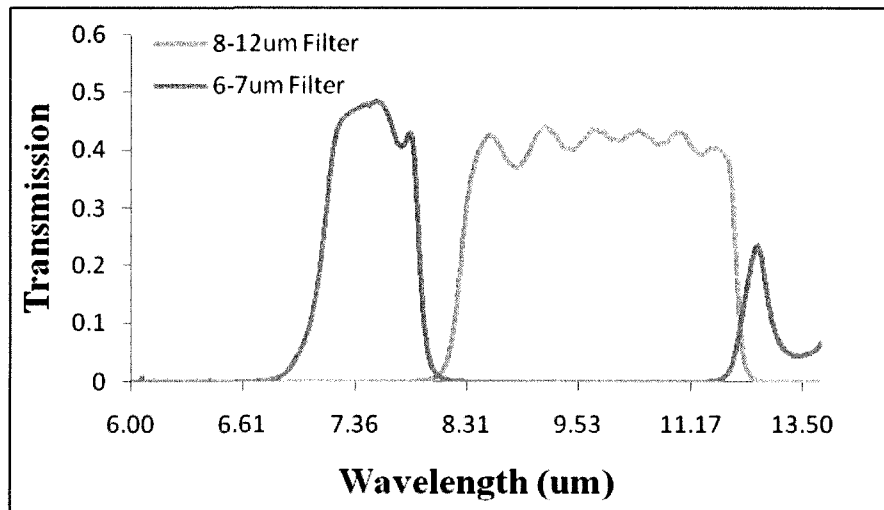


**Figure 4.9:** Transmission of bandpass optical filters

The photoresponsivity  $\mathfrak{R}$  can be written as:

$$\mathfrak{R} = I_{ph} / P_{in}, \quad (4.2)$$

Where  $I_{ph}$  is the photo current and  $P_{in}$  is the optical power incident of the detector. The photocurrents were measured by modulating the filtered blackbody infrared source using a mechanical chopper at a frequency of 1000 Hz, and collecting the signal using the low-noise current preamplifier and the FFT spectrum analyzer to get the photocurrent signal at 1KHz. . The effective received incident powers  $P_{in}$  of the 6-8  $\mu\text{m}$  and 8-12  $\mu\text{m}$  bands were calculated to 10.6 nW and 5.4 nW, respectively. Figure 4.10 shows the photoresponsivity  $\mathfrak{R}$  as function of bias voltages for these two bands at 78 K. At high bias magnitude ( $|V| > 0.5$  V), the 8-12  $\mu\text{m}$  band shows higher photoresponsivity than that of the 6-8  $\mu\text{m}$  band. A high photoresponsivity of 0.9 A/W was obtained at the bias voltage of -1.0 V. This is around ten times higher than that of the 6-8  $\mu\text{m}$  band at the same bias. At low bias magnitude ( $|V| < 0.5$  V), the 6-8  $\mu\text{m}$  band shows around five times higher photoresponsivity than that of the 8-12  $\mu\text{m}$  band.

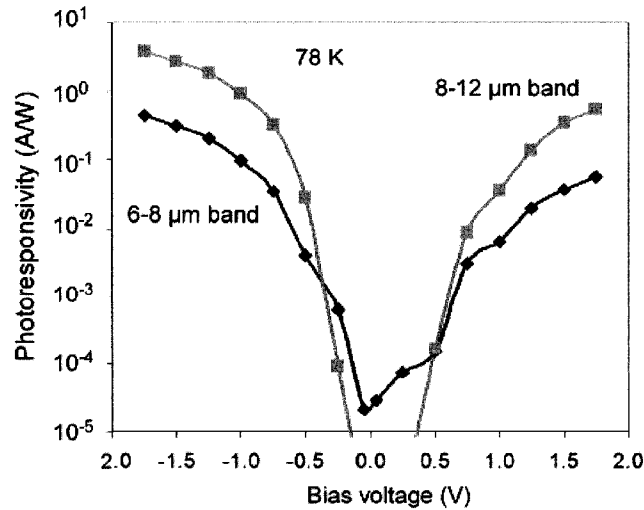


**Figure 4.10:** Responsivity as a function of bias voltage for each band

#### 4.6 DETECTIVITY

The specific photodetectivity  $D^*$  can be written as:

$$D^* = \frac{\Re\sqrt{A}}{i_{noise}}, \quad (4.4)$$

Where,  $A$  is the detector area, and  $i_{noise}$  is the noise current in  $A/Hz^{1/2}$  measured using the SR760 FFT spectrum analyzer. Figure 5 shows the calculated photodetectivity  $D^*$  at various bias voltages for these two bands. Peak photodetectivities of  $2.3 \times 10^9$  and  $1.6 \times 10^8 \text{ cmHz}^{1/2}/W$  at a bias of  $-1.5V$  were obtained for the  $8-12 \mu m$  and the  $6-8 \mu m$  bands, respectively. At a low bias of  $0.25 V$ , photodetectivities were calculated to be  $2.0 \times 10^8$  and  $< 1.0 \times 10^7$   $\text{cmHz}^{1/2}/W$  for the  $6-8 \mu m$  and the  $8-12 \mu m$  bands, respectively. The over ten times  $D^*$  difference indicates good band selectivity can be achieved by controlling the bias voltages.

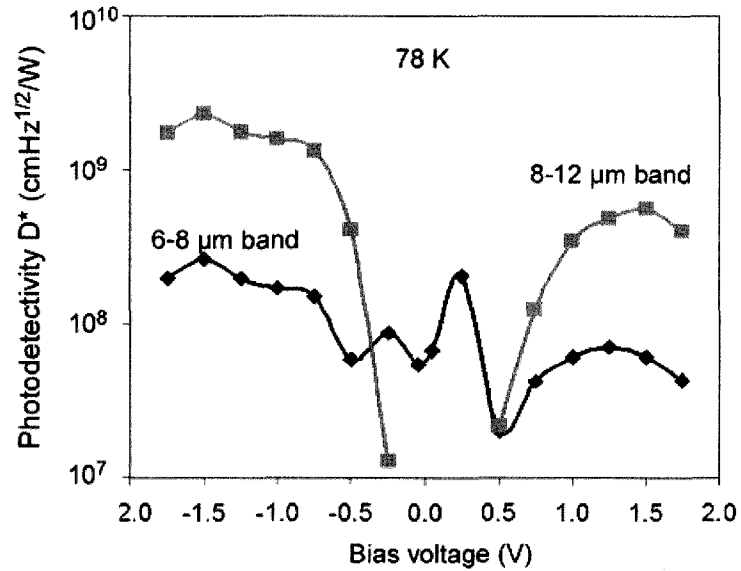


**Figure 4.11:** Detectivity as a function of bias voltage for each band

## **VI SUMMARY OF RESULTS**

A voltage-tunable dual band QDIP was demonstrated based on vertically-stacked InAs quantum dots layers with GaAs and  $\text{In}_{0.15}\text{Ga}_{0.85}\text{As}$  capping layers. The QDIP shows two IR detection bands peaked at  $\sim 7.7 \mu\text{m}$  and  $10.2 \mu\text{m}$ , corresponding to the GaAs and  $\text{In}_{0.15}\text{Ga}_{0.85}\text{As}$  capping layers, respectively. By tuning the bias voltage, the two bands can be individually or simultaneously turned on with around ten times photoresponsivity and peak photodetectivity differentiation. Since each of the detection bands can be designed individually, the vertically-stacked QDIP structure offers flexibility in detection band engineering and allows easy control of detection bands. The vertical stacked structure can be readily scaled up for multi-band detections.

## VII LITERATURE CITED

1. E.Towe, D. Pan, "Semiconductor Quantum Dot Nanostructures: Their Application in a New Class of Infrared Photodetectors," *IEEE Journal of Selected Topics in Quantum Electronics*, vol. 6(3), pp. 408-421, 2000.
2. R.G. Driggers, "Introduction to Infrared and Electro-Optical Systems," Artech House, Boston, 1999.
3. General Accounting Office (GAO), Missile Defense: Review of Results and Limitations of an Early National Missile Defense Flight Test, GAO-02-124, February 2002.
4. D. A. Reago, S. Horn, J. Campbell, R. Vollmerhausen, "Third generation imaging sensor system concept," *Proc. SPIE*, vol. 3701, pp. 108, 1999.
5. S. D. Guanpala and S. V. Bandara, "Quantum Well Infrared Photodetector Focal Plane Arrays", *Semiconductors and Semimetals*, vol. 62, pp. 197-282, 2000.
6. J. M. Mooney, V. E. Vickers, M. An and A. K. Brodzik, "High-throughput hyperspectral infrared camera," *J. Opt. Soc. Am. A*, vol. 14, pp. 2951, 1997.
7. S. Ghosh, et al, "Nonlinear optical and electro-optic properties of InAs/GaAs self-organized quantum dots," *J. Vac. Sci. Technol. B*, vol. 19, pp. 1455, 2001.
8. R.J. Keyes, "Optical and Infrared Detectors," Springer-Verlag, New York, 1977.
9. E. Theocharous, J. R. Birch, "Detectors for mid- and far-infrared spectrometry: selection and use," *Handbook of Vibrational Spectroscopy Volume 1: Theory and Instrumentation.*, John Wiley & Sons Ltd, UK , Vol. 1, pp. 1-19, 2002
10. E. Theocharous, N. P. Fox, and T. R. Prior, "Comparison of the performance of infrared detectors for radiometric applications," *Proc. SPIE*, vol. 2815, pp. 56, 1996.

11. P. E. Petersen, "Auger recombination in mercury cadmium telluride," in *Semiconductors and Semimetals*, R. K. Willardson and A. C. Beer, eds. (Academic, 1981), Vol. 18, Chap. 4, pp.121–155.
12. B. F. Levine, "Quantum-well infrared photodetectors," *J. Appl. Phys.* Vol. 74, no. 8, pp. R1-R81 (1993).
13. X. Jiang, S. Li, and M. Tidrow, "Investigation of a multistack voltage tunable four color quantum well infrared photodetector for mid and long wavelength infrared detection," *IEEE J. Quantum Electron.*, vol. 35, pp. 1685–1692, Nov. 1999.
14. G. Hasnain, B. F. Levine, C. G. Bethea, R. A. Logan, J. Walker, and R. J. Malik, "GaAs/AlGaAs multiquantum well infrared detector arrays using etched gratings," *Appl. Phys. Lett.* Vol. 54, pp. 2515, 1984.
15. D. Pan, E. Towe, and S. Kennerly "Normal-incidence intersubband (In, Ga)As/GaAs quantum dot infrared photodetectors," *Appl. Phys. Lett.*, vol. 73, pp. 1937-1939, 2003.
16. Z. Chen, O. Baklenov, E. T. Kim, I. Mukhametzhanov, J. Tie, and A. Madhukar, Y. Ye and J.C. Campbell, "Normal incidence InAs/Al<sub>x</sub>Ga<sub>1-x</sub>As quantum dot infrared photodetectors with undoped active region," *J. Appl. Phys.* 89, pp. 4558, 2001.
17. A. Stiff, S. Krishna, P. Bhattacharya, and S. Kennerly, "High-detectivity normal-incidence, midinfrared (4μm) InAs/GaAs quantum dot detector operating at 150 K," *Appl. Phys. Lett.*, vol. 79, pp. 421–423, 2001.
18. E. Kim, A. Madhukar, Y. Ye and J.C. Campbell, "High detectivity InAs quantum dot infrared photodetectors," *Appl. Phys. Lett.* Vol. 84, pp. 3277, 2004.
19. U. Bockelmann and G. Bastard, "Phonon scattering and energy relaxation in two-, one-, and zero-dimensional electron gases," *Phys. Rev. B* 42, p. 8947, 1990.

20. Z. Ye, J. C. Campbell, Z. Chen, E.-T. Kim, and A. Madhukar, "Noise and photoconductive gain in InAs quantum-dot infrared photodetectors," *Appl. Phys. Lett.*, vol. 83, pp. 1234–1236, 2003.
21. H. Lim, S. Tsao, W. Zhang, and M. Razeghi, "High-performance InAs quantum-dot infrared photodetectors grown on InP substrate operating at room temperature," *Appl. Phys. Lett.*, vol. 90, pp. 131112, 2007.
22. A. Stiff, S. Krishna, P. Bhattacharya, and S. Kennerly, "High-detectivity normal-incidence, midinfrared (4 $\mu$ m) InAs/GaAs quantum dot detector operating at 150 K," *Appl. Phys. Lett.*, vol. 79, pp. 421–423, 2001.
23. S. Tang, C. Chiang, P. Weng, Y. Gau, J. Luo, S. Yang, C. Shih, S. Lin, and S. Lee, "High-Temperature Operation Normal Incident 256 $\times$ 256 InAs–GaAs Quantum-Dot Infrared Photodetector Focal Plane Array," *IEEE Photon. Technol. Lett.*, vol. 18, no. 8, pp. 986–988, 2006.
24. Seongsin M. Kim, and James S. Harris, "Multicolor InGaAs Quantum-Dot Infrared Photodetectors," *IEEE Photon. Tech. Letts*, Vol. 16, pp. 2538, 2004.
25. Z. Ye, J. C. Campbell, Z. Chen, E.-T. Kim, and A. Madhukar, "Voltage-controllable multiwavelength InAs quantum-dot infrared photodetectors for mid- and far-infrared detection," *Appl. Phys. Letts*, vol. 92, pp. 4141-4143, 2002.
26. S. Krishna, D. Forman, Senthil Annamalai, P. Dowd, P. Varangis, T. Tumolillo, Jr, A. Gray, J. Zilko, K. Sun, M. Liu J. Campbell, and D. Carothers, "Demonstration of a 320 $\times$ 256 two-color focal plane array using InAs/InGaAs quantum dots in well detectors," *Appl. Phys. Letts*, vol. 86, pp. 193501, 2005.



27. D. A. B. Miller, D. S. Chemla, T. C. Damen, A. C. Gossard, W. Wiegman, T. H. Wood, and C. A. Burrus, *Phys. Rev. B*, vol. 32, pp.1043-1060, 1985.